3. THE DATA ANALYSIS

In this chapter, the complete data analysis is presented, from the raw data to the measurement of the form factor. Given the small cross section of the process under study, one of the main goals is an efficient selection of the events. Especially important is also an evaluation of the background sources; here the main discussion is given, while the details on how some quantities have been measured are given in the appendices.

3.1 Selection of $\bar{p}p \to e^+e^-$ Events

(a) Data Sample

The data taken during E-835 are distributed in the energy region 2.9 GeV $< \sqrt{s} < 4.3$ GeV. To reduce background contamination, I exclude the data taken in proximity of some resonances, because they are known to yield a comparatively strong e^+e^- or J/ψ-inclusive signal (with the J/ψ decaying into e^+e^-); namely[a] the J/ψ (rest energy m = 3096.88 MeV, full width Γ = 87 keV), the χ_0 (m = 3417 MeV, Γ = 14 MeV), the χ_1 (m = 3510.5 MeV, Γ = 0.9 MeV), the χ_2 (m = 3556.2 MeV, Γ = 2.0 MeV) and the ψ' (m = 3686.00 MeV, Γ = 0.28 MeV). These data are useful for tuning the selection, and for efficiency and background studies. The remaining data ($\approx 10^2$ pb^{-1}) have been grouped in the way indicated in Table 3.1. For each

[a] Masses and widths are taken from the Review of Particle Physics (Caso et al. 1998).

data point, the weighed mean $\sqrt{s}$ and rms, the total integrated luminosity L and the number N of events (selected according to the criteria described in Section 3.1.(c)) are reported. Figure 3.1 shows the distribution of the accumulated luminosity versus the CM energy, emphasizing the samples that I use in the analysis with a horizontal shaded bar.

(b) First-level Trigger and On-line Filter

The trigger logic that selects events for this analysis requires two back-to-back electron tracks and, independently, two calorimeter showers with high invariant mass.

A charged track (h) is defined as a coincidence between an element of hodoscope H1 and one of the four corresponding elements of hodoscope H2 (Figure 3.2), plus two overlap H2 elements. So, for instance, element H1-2 is in coincidence with the logical OR of elements H2-4 to H2-9. If a hit is also recorded in the appropriate cells of the Čerenkov counter, an electron track (e) is defined.

Sample	$\sqrt{s}$ Interval (GeV)	Mean ± Rms (GeV)	L (pb^{-1})	N
1	2.900–3.050	2.9737 ± 0.0269	17.69	93
2	3.200–3.340	3.2840 ± 0.0427	1.78	3
3	3.520–3.540	3.5261 ± 0.0035	47.84	33
4	3.570–3.670	3.6208 ± 0.0241	33.99	14
5	3.710–3.880	3.7889 ± 0.0664	1.86	1
6	4.270–4.310	4.2890 ± 0.0003	0.76	0

Tab. 3.1: Summary of data used for the form factor analysis.

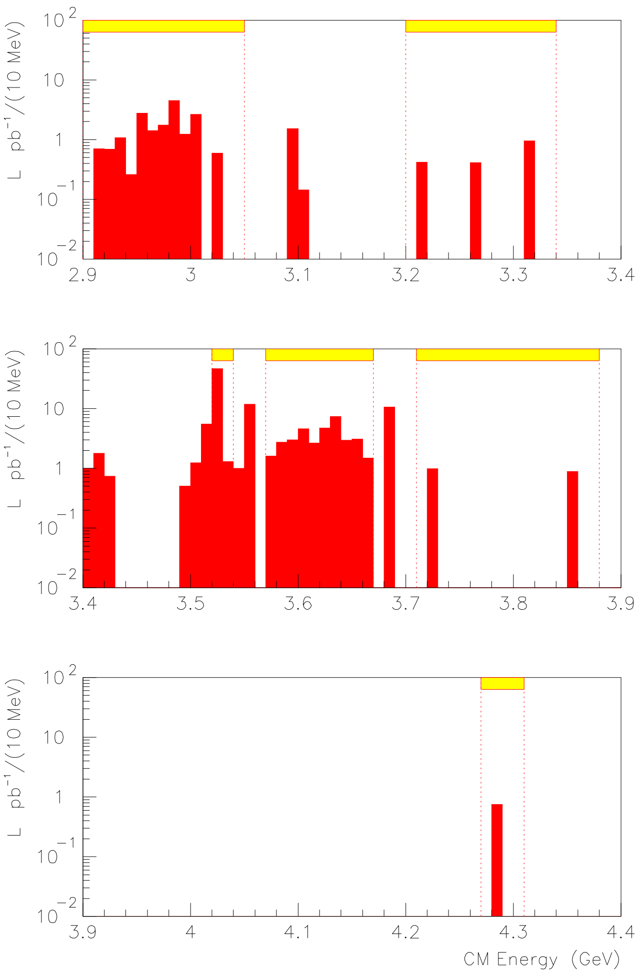

Fig. 3.1: Distribution of the luminosity accumulated during E-835 as a function of CM energy.

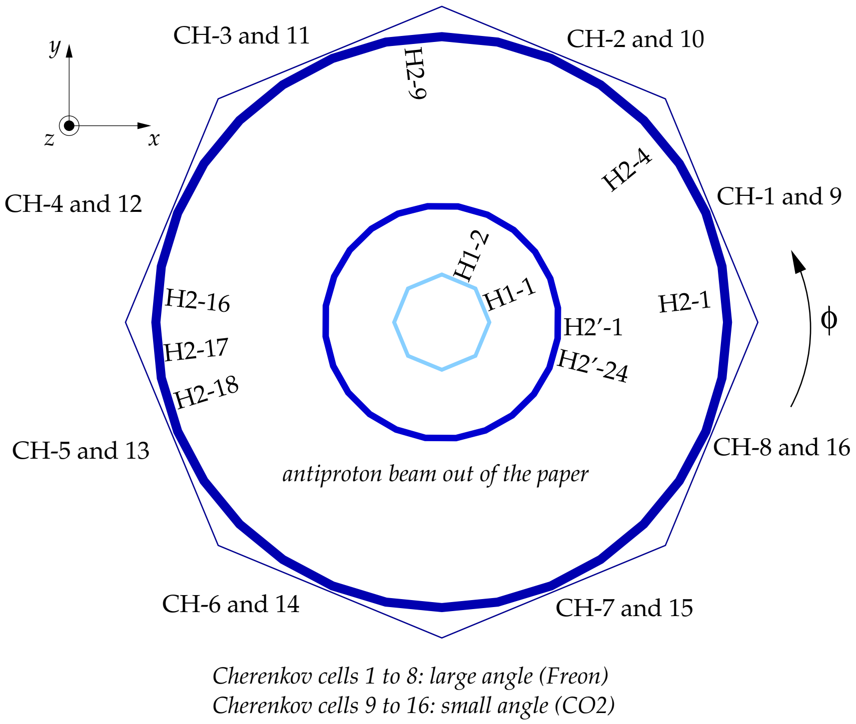

Fig. 3.2: Schematic diagram of the counters employed in the trigger.

The charged coplanarity logic (COPL) is formed by the elements of hodoscope H2 and selects tracks that are back-to-back in ϕ. It is the coincidence between an H2 element and at least one of the three opposite in azimuth. For example, elements H2-1 with the logical OR of elements H2-16, H2-17 and H2-18.

The central calorimeter is used to tag events with two back-to-back large energy deposits, separated by at least 90° in azimuth (PBG3 logic). The signals from the 1280 lead glass blocks first go through the Level I Summers, where, for each ring[b], the signals of nine consecutive blocks are summed (Figure 3.3). The first and last block in the sum are overlap blocks, ie they are counted in two adjacent sets of nine blocks. For instance, in ring 1, the signals from blocks 1 to 9 are summed, as are 9 to 17, etc.; finally, blocks 57 to 64 back to (and including) block 1. Thus, 160 signals leave the Level I Summers, eight from each ring. These signals are then split; one set forms the strobe for the logic units (Memory Look-up Units, or MLUs), and the other set enters the Level II Summers.

At the Level II Summers, the signal from each octant of blocks is summed with the same octant in five (or four) other adjacent rings. For example, octant 1 (ie wedges 1 to 9) from rings 1 to 4 are summed, as are the ones from rings 4 to 8, etc.; finally, from rings 16 to 20. It should be noticed that the first sum is made from only four rings, and that there is again an overlap (of rings this time). The 40 signals that leave the Level II Summers are the signals of the 40 so-called "super-blocks" of the central calorimeter.

After Level II, the 40 signals are split. One set goes to ADCs and the other set goes to an integrator. After the integrator, the signals enter a discriminator, whose thresholds are set according to two-body reactions ($\bar{p}p \rightarrow \gamma\gamma$ below the J/ψ formation energy, $\bar{p}p \rightarrow J/\psi(\rightarrow e^+e^-) + X$ above);

[b] The definitions and pictures of the 20 rings and of the 64 wedges are in Section 2.3.(a).

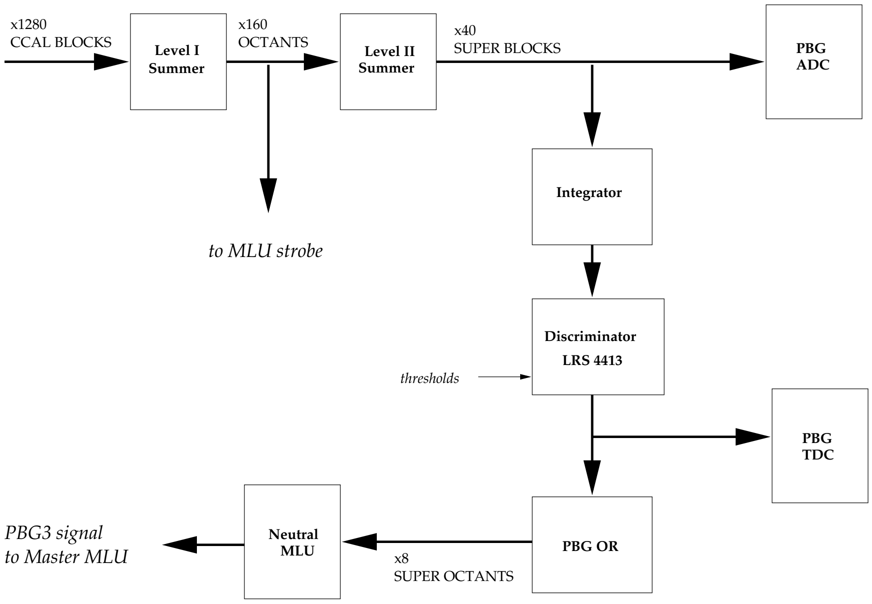

Fig. 3.3: The two-body branch of the CCAL trigger logic, from the individual blocks to the final PBG3 signal.

therefore, they depend on the CM energy at which the data is taken.

The 40 super-block signals are split again after the discriminator; one set going to TDCs and the other set going to the PBG OR module. This module performs the logical OR of the five super-blocks in the same octant. Its 8 outputs are fed into the Neutral MLU, which looks for coincidences between one of the eight octants and the three opposite to it in azimuth (for instance octant 1 and at least one among octants 4, 5 and 6). The resulting logic signal is called PBG3, which stands for "lead glass, one versus three".

The final e^+e^- trigger is formed by three branches. The first one is the main logic; the other two are used to check the efficiency of the Čerenkov counter and of PBG3 logic. In symbols:

$$\begin{aligned}(e^+e^-) \quad = \quad & (2e)\cdot(\mathrm{H2}\leq 4)\cdot(\mathrm{PBG3}) \quad + \\ & (1e)\cdot(2h)\cdot(\mathrm{H2}=2)\cdot(\mathrm{COPL})\cdot(\mathrm{PBG3}) \quad + \\ & (2e)\cdot(\mathrm{H2}=2)\cdot(\mathrm{COPL})\cdot(\overline{\mathrm{FCH}}).\end{aligned} \tag{3.1}$$

The symbols $(\mathrm{H2} = 2)$ and $(\mathrm{H2} \leq 4)$ refer to the multiplicity (ie number of hits) in hodoscope H2, while $\overline{\mathrm{FCH}}$ represents the veto on the forward hodoscope.

Events which satisfy the hardware trigger are processed by the on-line filter[c], which requires the event to contain at least one pair of CCAL clusters forming an invariant mass greater than 2.2 GeV (2.0 GeV when taking data below the transition energy of the accumulator).

(c) Data Reduction and Off-line Selection

Electron tracks are reconstructed off-line by associating the hits in the counters (hodoscopes and Čerenkov detector) with the calorimeter showers. Track information from the inner detectors is added to improve the angular

[c] The filter is called PRUDE, which stands for Program Rejecting Unwanted Data Events.

resolution. The two electron candidates are identified as the tracks with the highest invariant mass.

The off-line selection of $\overline{p}p \to e^+e^-$ events is based upon two straightforward criteria: identification of the electron and of the positron and kinematic characteristics of the event. In the following paragraphs, I describe in detail the cuts that I impose on electron identification, on CCAL cluster multiplicity, on kinematic fit probability and on fiducial volume.

Fiducial volume. The cut in fiducial volume is necessary in order to remove inhomogeneities in the response of the detector at its edges. For this reason I accept only events in which both electron candidates have polar angles in the interval $15° < \theta < 60°$, well within the angular coverage of the central detector.

Electron identification. What characterizes electrons and positrons in the E-835 detector is pulse height in the Čerenkov counter, energy loss in the hodoscopes and profile of the electromagnetic shower. For each candidate electron track, an electron weight index (EW) is constructed using the pulse heights in the counters and the shape of the electromagnetic shower (Patrignani 1997). The particles that we wish to reject are mostly coalescing e^+e^- pairs (from photon conversions or Dalitz decays of neutral pions), coalescing photons from π^0 decays and hadrons. Following is the complete list of the variables used. The pulse heights in the counters are aimed at discriminating between singly charged tracks and coalescing e^+e^- pairs:

- pulse height p_1 in hodoscope H1 (in mips, ie normalized to the signal generated by a minimum-ionizing particle);
- pulse height p_2 in hodoscope H2 (in mips);

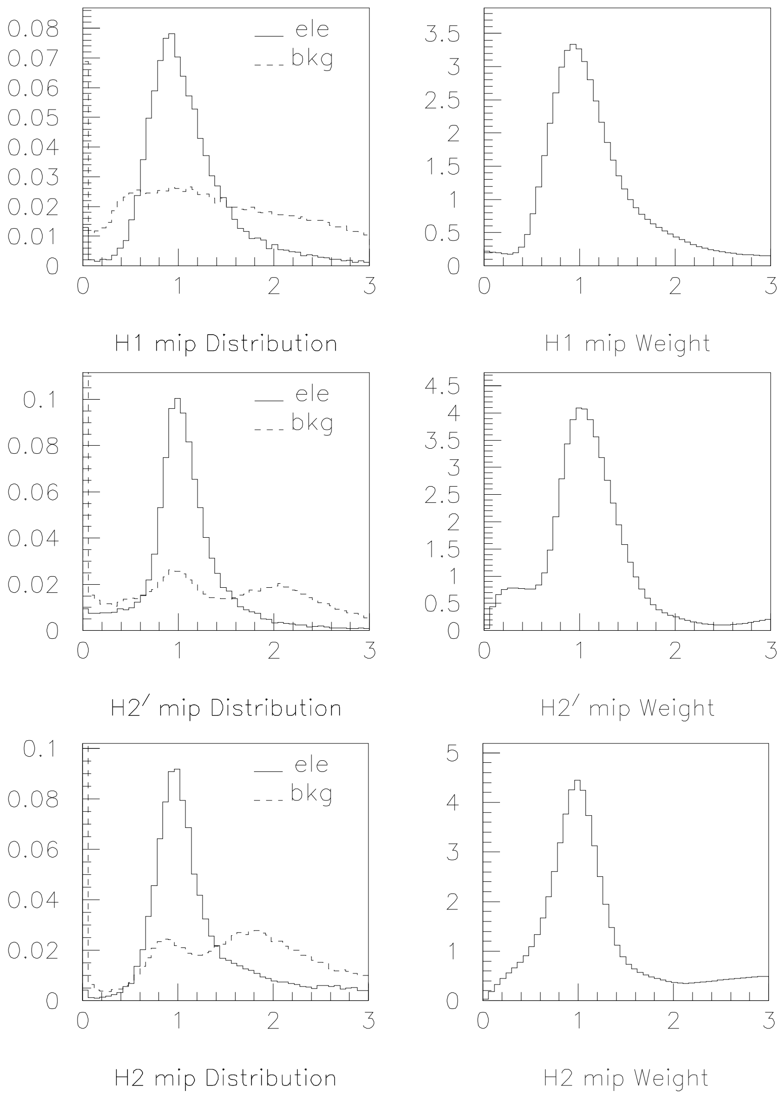

Fig. 3.4: Electron-Weight distributions for the three hodoscopes.

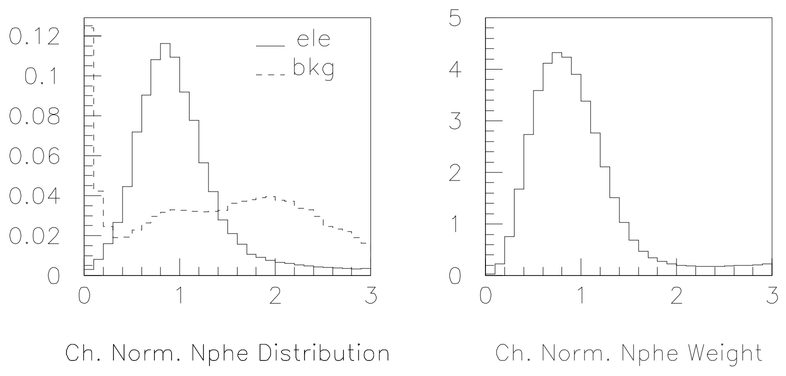

Fig. 3.5: Electron-Weight distributions for the Čerenkov counter.

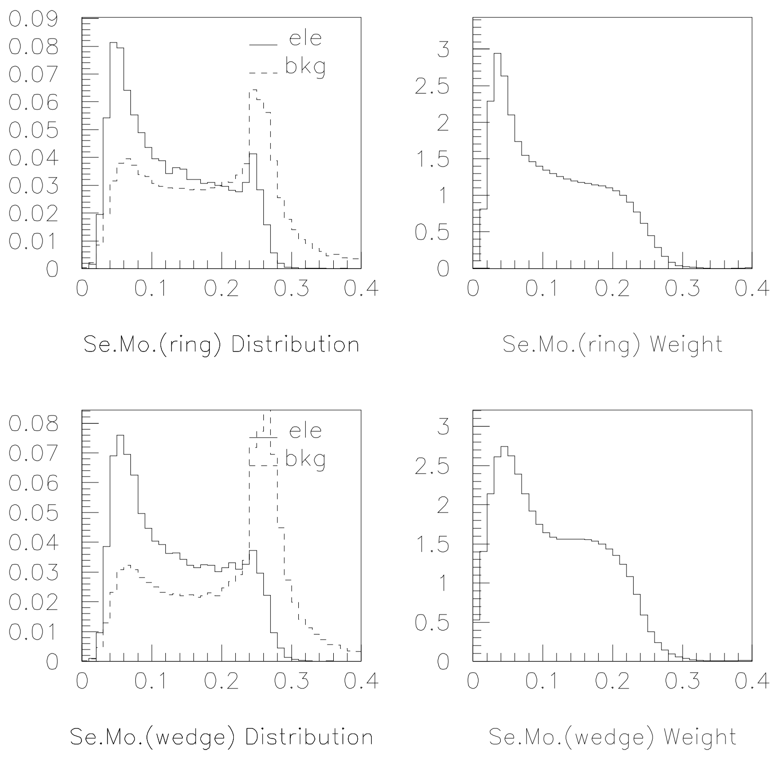

Fig. 3.6: Electron-Weight distributions of CCAL second moments.

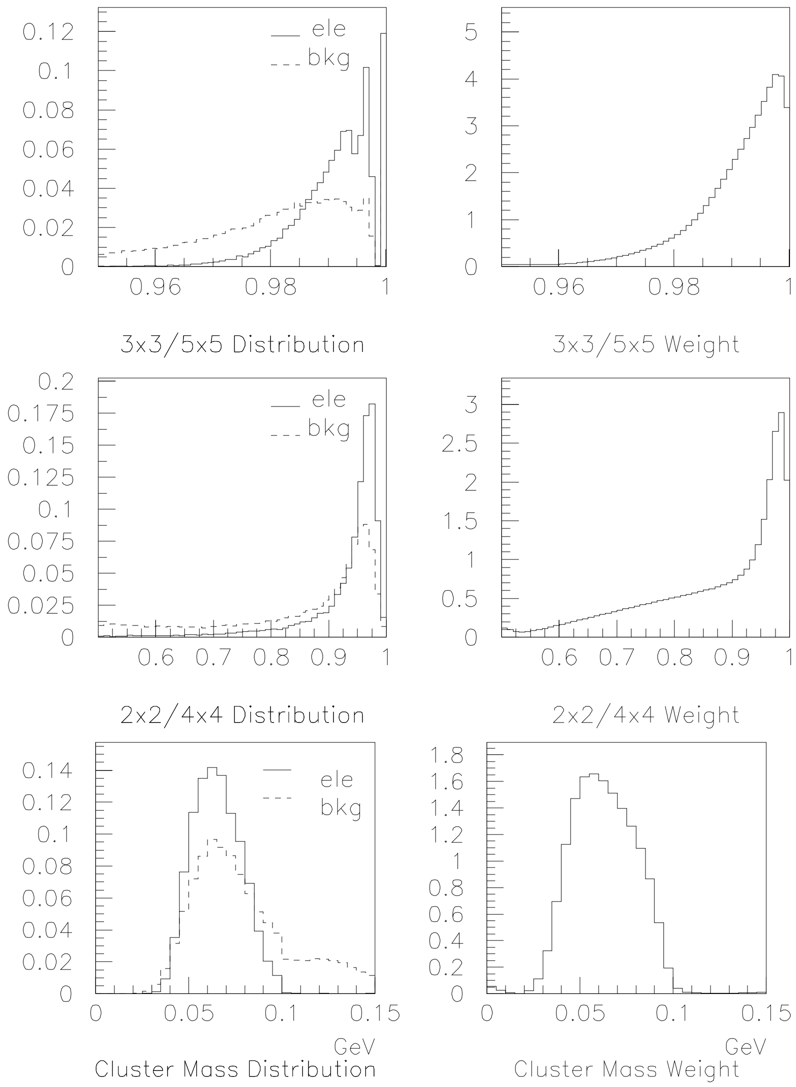

Fig. 3.7: Electron-Weight distributions of CCAL fractional shower energy and cluster mass.

- pulse height p_p in hodoscope H2′ (in mips);
- pulse height p_C in the Čerenkov counter (normalized number of photoelectrons);

coalescing e^+e^- or $\gamma\gamma$ pairs generate in the CCAL a wider electromagnetic shower, compared to single electrons, positrons or photons. Moreover, the distribution of the energy deposits in the blocks can have two local maxima. Most of the times, hadrons release a small amount of energy (≈ 450 MeV) in only one block (punch-through tracks); if a nuclear interaction takes place which generates neutral pions in the final state, an electromagnetic shower is inititated, but it is usually asymmetric. The following parameters are used to characterize the energy deposits in the calorimeter:

- second moments of the energy distribution $E(r,w)$ in the CCAL cluster, within a 3×3 grid around the highest-energy block (r_0, w_0), expressed in ring (r) and wedge (w) units:

$$s_r \equiv \sum_{(r,w)\in 3\times 3} E(r,w)\cdot(r-r_0)^2 \Bigg/ \sum_{(r,w)\in 3\times 3} E(r,w)$$

$$s_w \equiv \sum_{(r,w)\in 3\times 3} E(r,w)\cdot(w-w_0)^2 \Bigg/ \sum_{(r,w)\in 3\times 3} E(r,w);$$

- fractional shower energy in a 3×3 block region surrounding the highest energy block, with respect to a 5×5 grid; same thing for a 2×2 grid (defined by the highest energy block and by the largest deposit among the eight adjacent to it) with respect to the 4×4 region enclosing it:

$$R_{3/5} \equiv \sum_{(r,w)\in 3\times 3} E(r,w) \Bigg/ \sum_{(r,w)\in 5\times 5} E(r,w)$$

$$R_{2/4} \equiv \sum_{(r,w)\in 2\times 2} E(r,w) \Bigg/ \sum_{(r,w)\in 4\times 4} E(r,w)$$

- cluster mass, constructed from the energy deposits in the blocks within a 5×5 grid centered around the highest energy hit; it is defined as follows:

$$M_c \equiv \left[\left(\sum_{(r,w)\in 5\times 5} E(r,w) \right)^2 - \left(\sum_{(r,w)\in 5\times 5} E(r,w) \cdot \hat{x}(r,w) \right)^2 \right]^{1/2}, \tag{3.2}$$

where $\hat{x}(r,w)$ is the unit vector from the interaction point to the center of the counter (r,w).

The distribution $f_i(x_i)$ $(x_i = p_1, p_2, \ldots, M_c)$ of each of the nine variables listed above is observed in a clean sample of electron and positron tracks ($J/\psi \to e^+e^-, \chi_{c1,2} \to J/\psi(\to e^+e^-)+\gamma$ and $\psi' \to J/\psi(\to e^+e^-)+X$, selected with a kinematic fit) and in a background sample (data taken off-resonance at various energies). The corresponding normalized distributions are called $f_i^{\mathrm{ele}}(x_i)$ and $f_i^{\mathrm{bkg}}(x_i)$, respectively; they are shown on the left side of Figures 3.4–3.7. On the right side of the same figures, the ratio ('weight'):

$$W_i = \frac{f_i^{\mathrm{ele}}(x_i)}{f_i^{\mathrm{bkg}}(x_i)} \tag{3.3}$$

is plotted for each of the nine chosen quantities.

For a track with a particular set of values $x_1, \ldots, x_9$ of the above mentioned variables, the EW index is defined as:

$$\mathrm{EW} \equiv \prod_i W_i \tag{3.4}$$

Since in a good event both candidates have to be good electron tracks, a sensible variable to use is the product of the EW indices of the two candidate electrons. The distribution of $\log_{10}(\mathrm{EW1} \cdot \mathrm{EW2})$ in the electron and in the background samples is shown in Figure 3.8.

In order to reduce the size of the data sample, a preliminary selection is applied to the raw data by imposing a loose cut on the product of the EW in-

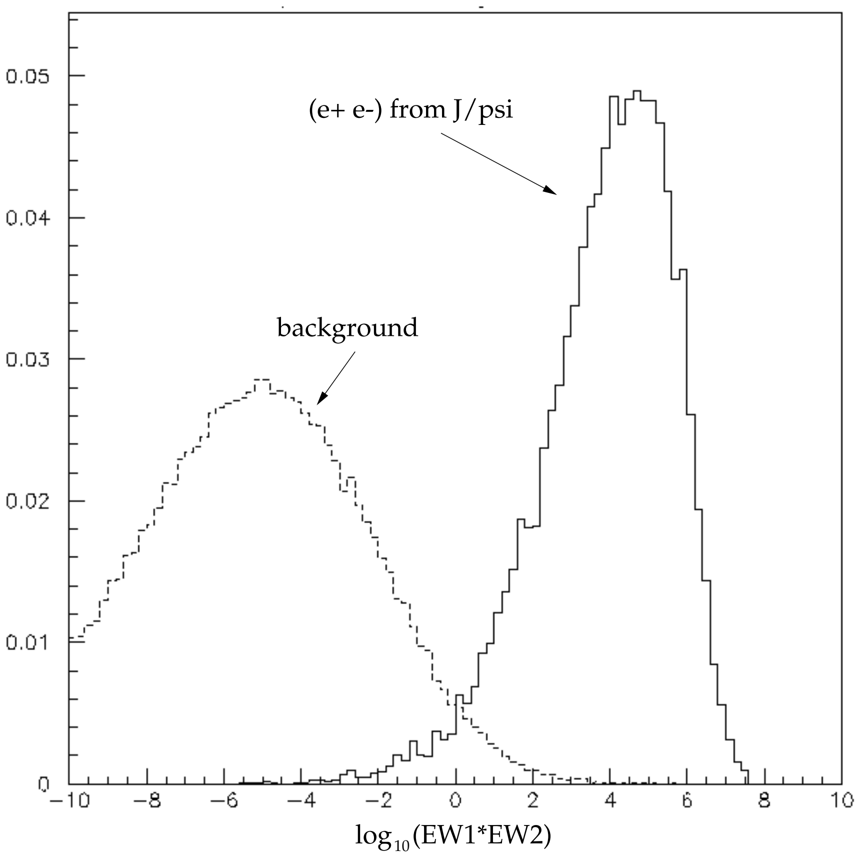

Fig. 3.8: Distribution of EW indices′ product for electrons and background.

dices for the two electron candidates: $\log_{10}(EW1 \cdot EW2) > -1$. Only events which pass this preliminary selection undergo the subsequent analysis. In the final selection, I cut at $\log_{10}(EW1 \cdot EW2) > 0$.

CCAL multiplicity. The simplest requirement on the number of clusters in the calorimeter would be exactly two on-time clusters. The definition of 'on-time' is tuned on a clean $J/\psi \to e^+e^-$ sample. Figure 3.9a shows the time distribution of the clusters associated with clean electrons and positrons. The horizontal scale has an arbitrary software offset. The time of a cluster is defined as the TDC reading of the highest energy block. In Figure 3.9b, I plot the fraction of electron or positron tracks with cluster times within a window of half-width Δt centered around the mean value $\langle t \rangle$, as a function of Δt. In this analysis, extra clusters whose times differ from the

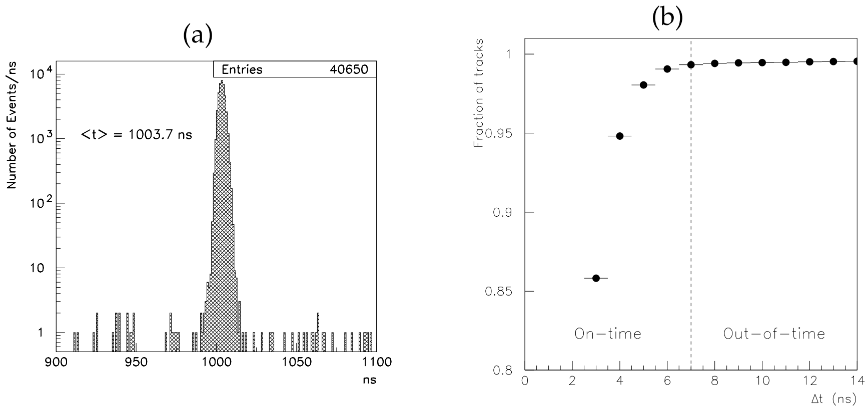

Fig. 3.9: (a) Time distribution of clean electron and positron tracks from $J/\psi \to e^+e^-$. The horizontal scale has an arbitrary software offset. (b) Fraction of tracks from Figure (a) within a window centered around the mean, as a function of the window's half-width. The vertical dashed line marks the chosen definition of 'on-time' for extra clusters.

average electron or positron time by less than 7 ns are classified as 'on-time'.

An electron or positron, by interacting with the detector material, can radiate a Bremsstrahlung photon, which might form a distinct satellite cluster in the CCAL. The thicker devices on the particles' path are the beam pipe and the silicon pads; the effect is of the order of a few percent.

To avoid rejecting these events, I do not impose a strict cut demanding exactly two on-time clusters. Events with more on-time clusters are kept, provided that the extra clusters, when paired with either electron candidate, give an invariant mass below 100 MeV. This value has been tuned on a J/ψ sample selected with a tight Electron-Weight cut (Figure 3.10a). In Figure 3.10b, the electron/extra-cluster invariant mass distribution is shown for background events; the π^0 peak is prominent.

Any number of out-of-time or undetermined clusters is allowed. The invariant mass formed by the candidate electron and by the possible out-of-time or undetermined clusters is checked (to make sure that there is no

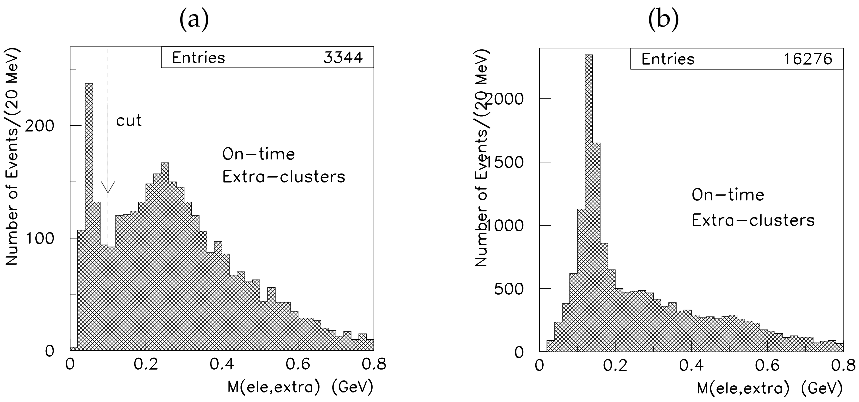

Fig. 3.10: Distribution of the invariant mass formed by all on-time extra clusters when paired with the closest candidate electron: (a) at the J/ψ energy (after imposing a tight cut on the EW index) and (b) at $\sqrt{s}$ = 3.0 GeV (no cuts besides the preliminary selection).

π^0 contamination), but not cuts are necessary.

Kinematic fit. The goodness of the two-body hypothesis is tested by means of a four-constraint kinematic fit. All candidate events are tested with this hypothesis and are accepted if the fit probability is above 1%. In Figure 3.11 is the fit probability distribution for e^+e^- decays of the J/ψ selected by means of the Electron-Weight ($\log_{10}(EW1 \cdot EW2) > 1$), the CCAL multiplicity (allowing low invariant mass satellite clusters) and the fiducial volume cuts.

The number N of events that satisfy all the criteria described so far is reported in Table 3.1 for each energy region.

3.2 Estimate of Selection Efficiencies

The overall efficiency ε is the product of the trigger efficiency ε_{tri}, the efficiency of the preliminary selection ε_{pre} and that of the off-line analysis ε_{ana}:

$$\varepsilon = \varepsilon_{tri} \cdot \varepsilon_{pre} \cdot \varepsilon_{ana}.$$

The inefficiency of the on-line filter is negligible.

The trigger efficiency ε_{tri} takes into account the detection efficiency of the detectors involved in the formation of the logic signals and the efficiency of the logic itself. It has been measured at the J/ψ energy with a special trigger run, since all three branches of the normal trigger require two tracks (Equation 3.1). The special trigger required only one electron track in the H1, H2 and Čerenkov counters (1e), in addition to PBG3, the two-cluster requirement in the central calorimeter. The result is ε_{tri} = 0.898±0.005(stat) (Baldini and Marchetto 1997).. The efficiency of the PBG3 logic can be checked on every run, because the third branch of the e^+e^- trig-

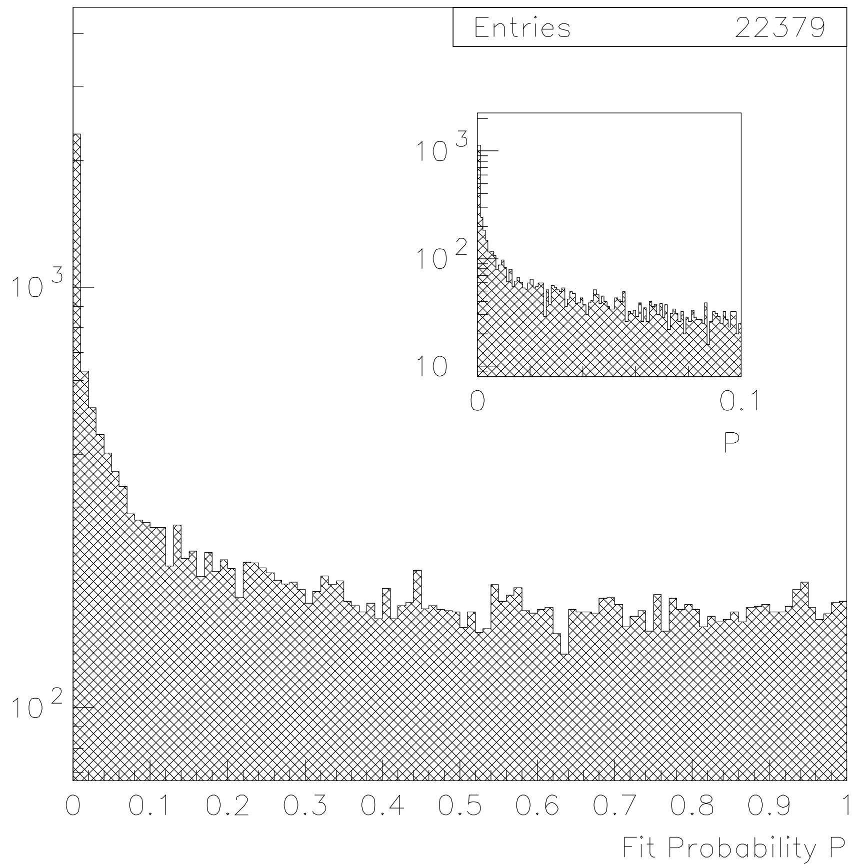

Fig. 3.11: Probability distribution of the kinematic fit for clean $J/\psi \rightarrow e^+e^-$. In the inset is a blow-up of a portion of the horizontal scale (the binning is ten times finer).

ger does not require it (Equation 3.1). Its inefficiency turns out to be negligible.

The efficiency of the preliminary off-line cut $\log_{10}(\mathrm{EW1} \cdot \mathrm{EW2}) > -1$ has been measured using clean samples of $J/\psi \rightarrow e^+e^-$, $\chi_{c1,2} \rightarrow e^+e^-\gamma$ and $\psi' \rightarrow e^+e^-$ events (Patrignani 1998). It has been found to be $\varepsilon_{\mathrm{pre}} = 0.985 \pm 0.001(\mathrm{stat})\,^{+0.007}_{-0.020}(\mathrm{syst})$. The systematic error arises from the different processes and CM energies, and represents the maximum deviations observed from the average value.

I evaluated the efficiency of the second set of off-line cuts (the final selection) on both $J/\psi \rightarrow e^+e^-$ and $\psi' \rightarrow e^+e^-$ events, so as to be sensitive to possible energy-dependent systematic uncertainties. Also, the J/ψ and ψ' data samples have been broken down into four subsamples (runs 533–909, 1006–1432, 2003–2460 and 3005–3346), in order to check the stability of the efficiency over time and for different running conditions. The four subsam-

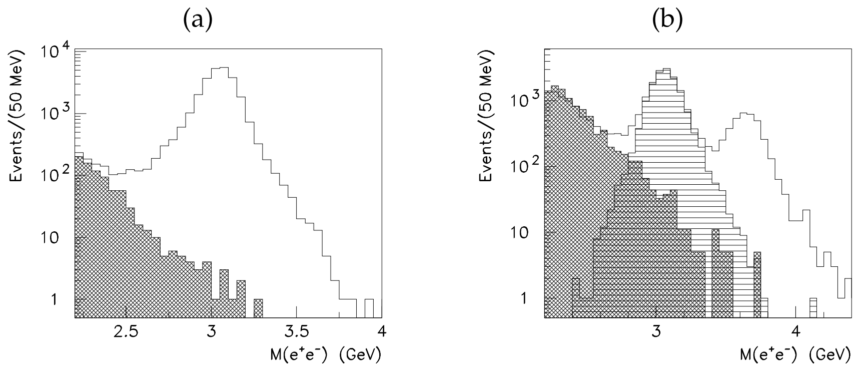

Fig. 3.12: Invariant mass distribution for candidate electrons after preliminary cuts only: (a) at the J/ψ formation energy (white) and at $\sqrt{s}$ = 3.3 GeV (cross-hatched); (b) at the ψ' formation energy (white, all events; horizontal lines, J/ψ-inclusive subsample) and at $\sqrt{s}$ = 3.8 GeV (cross-hatched).

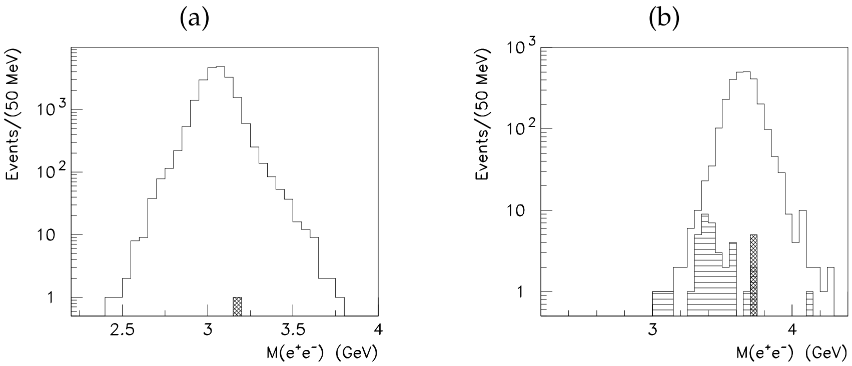

Fig. 3.13: Invariant mass distribution for candidate electrons after the complete selection: (a) at the J/ψ formation energy (white) and at $\sqrt{s}$ = 3.3 GeV (cross-hatched); (b) at the ψ′ formation energy (white, all events; horizontal lines, J/ψ-inclusive subsample) and at $\sqrt{s}$ = 3.8 GeV (cross-hatched).

Sample	J/ψ Energy		ψ′ Energy	
	Bkg @ 3.0 GeV	Bkg @ 3.3 GeV	Bkg @ 3.6 GeV	Bkg @ 3.8 GeV
1	0.780±0.004	0.789±0.004	0.72±0.01	0.72±0.01
2	0.789±0.005	0.806±0.005	0.75±0.02	0.75±0.02
3	0.728±0.006	0.737±0.005	0.77±0.01	0.77±0.01
4	0.786±0.009	0.801±0.009	0.77±0.02	0.77±0.02

Tab. 3.2: Efficiency of the off-line analysis calculated on different samples. The errors are statistical.

ples correspond to data taken in Oct–Dec 1996, Jan–Mar 1997, Apr–Jul 1997 and Jul–Sep 1997, respectively.

Figure 3.12 shows the invariant mass distribution for candidate electrons after preliminary cuts only: (a) at the J/ψ and (b) at the ψ' formation energies. The cross-hatched areas in both histograms show the background contamination in these samples, calculated by applying the same preliminary cuts to data taken off-resonance and rescaled by luminosity. In Figure 3.12b, inclusive $J/\psi + X$ events coming from the decay $\psi' \to J/\psi + X$ are also shown (horizontal lines). They are selected by means of a 1C kinematic fit on events with an identified e^+e^- pair in the final state ($\log_{10}(\mathrm{EW1} \cdot \mathrm{EW2}) > 0$), requiring that the fit probability be higher than 1%, with the additional requirement that the fit probability for the hypothesis $\psi' \to e^+e^-$ be less than 10%.

Figure 3.13 shows the corresponding distributions after the complete event selection. It can be seen that the background contamination in these data samples is very low.

The efficiency of the off-line analysis is defined as the fraction of events in the preliminary samples (Figure 3.12) that survive all cuts (Figure 3.13), once background (including $J/\psi + X$ events at the ψ') is subtracted. At the ψ', only events with invariant mass above 3.4 GeV are considered.

To estimate the systematic uncertainty introduced by the subtraction procedure, I employ background data taken both below and above resonance ($\sqrt{s} = 3.0$ GeV and $\sqrt{s} = 3.3$ GeV for the J/ψ, and $\sqrt{s} = 3.6$ GeV and $\sqrt{s} = 3.8$ GeV for the ψ').

The efficiency is found to be $\varepsilon_{\mathrm{ana}} = 0.764 \pm 0.003(\mathrm{stat})\ ^{+0.042}_{-0.048}(\mathrm{syst})$. Its value is the average of the sixteen efficiencies calculated with the same procedure on the various samples (Table 3.2): J/ψ or ψ' signal from one of the

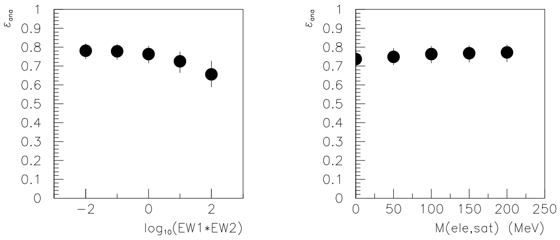

Fig. 3.14: Efficiency of the off-line selection as a function of each cut.

four sets of runs, subtracted background taken below or above resonance. The asymmetric systematic errors are the difference between the average and the largest and smallest values. The individual contributions are approximately 3% from CM energy and 1% from the choice of background; the rest comes from the choice of run numbers.

The overall efficiency, which I use to correct the number of events at all energies, is thus $\varepsilon = 0.676 \pm 0.005(\text{stat})\ ^{+0.042}_{-0.055}(\text{syst})$.

3.3 Stability of the Selection Criteria

The purpose of this study is to verify that the cuts chosen for the event selection, which are described in Section 3.1.(c), are optimized in terms of efficiency and background rejection.

Using the procedure described above in Section 3.2, I calculate the efficiency ε_{ana} of the off-line selection as a function of the three cuts employed: the product of the Electron-Weight indices, the maximum invariant mass allowed when combining a possible on-time extra clusters with the candidate electron or positron and the probability of the two-body kinematic fit (the presence of the fiducial volume cut is understood). While two of them are set to their chosen values, the third is allowed to vary between a 'loose' and a 'tight' value (arbitrarily defined). For instance, for the extra cluster invariant mass, the loose cut is 200 MeV/c^2, above the π^0 mass; whereas the tight cut is 0 MeV/c^2, which is equivalent to requiring no on-time extra clusters. The results are shown in Figure 3.14.

Also the number N of selected events is measured as a function of the three cuts. Figures 3.15, 3.16 and 3.17 show the results for the three samples where they are statistically more significant (samples 1, 3 and 4 in Table 3.1).

The ratio N/ε_{ana} as a function of the cuts indicates whether the sample is being contaminated by background and whether the efficiency of the selection is optimized. In the absence of background, N/ε_{ana} is expected to be flat.

I consider the plots in Figures 3.15–3.17 satisfactory. The ratio N/ε_{ana} is stable in proximity of the chosen cuts, and the selection criteria have both high efficiency and good background-rejection power.

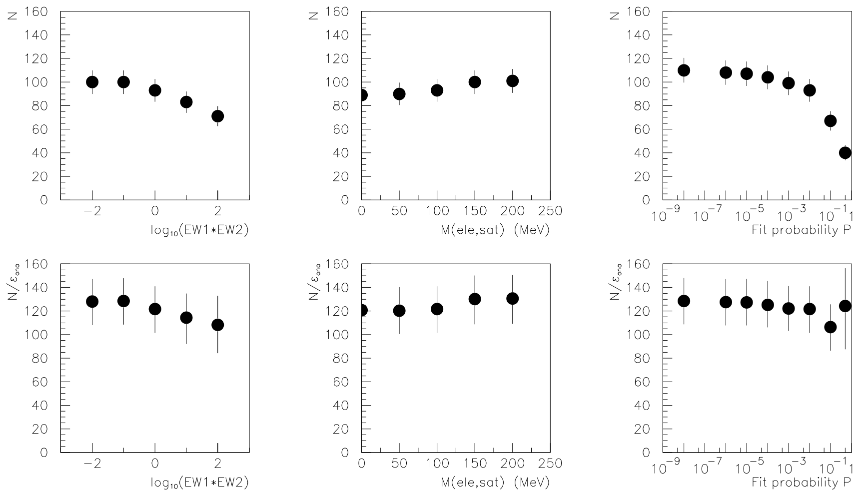

Fig. 3.15: The number of events N selected from sample 1 ($\sqrt{s}$ = 3.0 GeV) and the ratio N/ε_{ana} as a function of the off-line cuts.

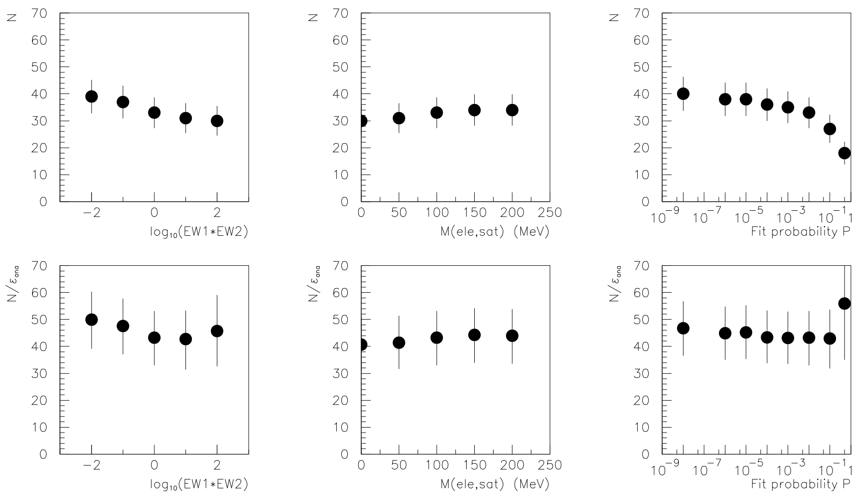

Fig. 3.16: The number of events N selected from sample 3 ($\sqrt{s}$ = 3.53 GeV) and the ratio N/$\varepsilon_{\mathrm{ana}}$ as a function of the off-line cuts.

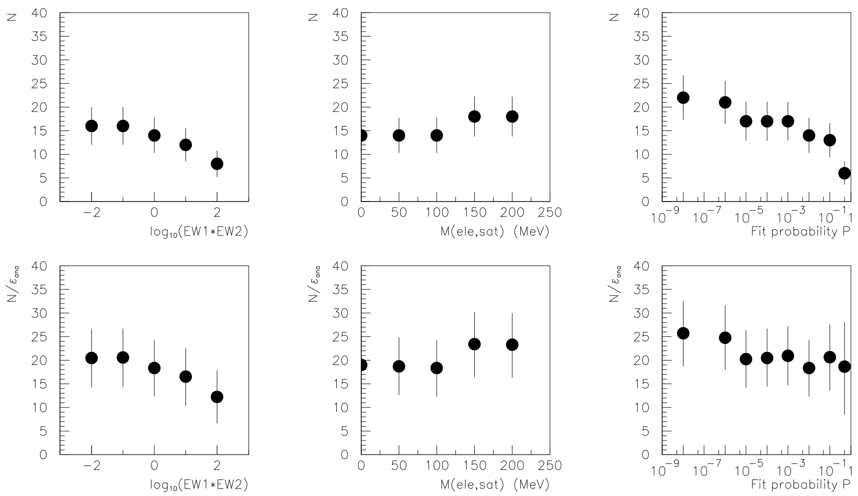

Fig. 3.17: The number of events N selected from sample 4 ($\sqrt{s}$ = 3.6 GeV) and the ratio N/$\varepsilon_{\mathrm{ana}}$ as a function of the off-line cuts.

3.4 Study of Background Processes

Since the e^+e^- signal is immersed in the comparatively huge $\bar{p}p$ total cross section, a thorough evaluation of the magnitude of background contamination is necessary. The reactions that can simulate a good signal in the E-835 detector are photon conversions, π^0 Dalitz decays, two-body hadronic final states (mainly $\pi^+\pi^-$) and inclusive production of J/ψ.

(a) Photon Conversions and Dalitz Decays

I consider the reactions:

$$\bar{p}p \rightarrow \pi^0\pi^0 \quad (3.5)$$

$$\bar{p}p \rightarrow \pi^0\gamma \quad (3.6)$$

$$\bar{p}p \rightarrow \gamma\gamma. \quad (3.7)$$

Two coalescing electron-positron pairs are generated if the two photons in reaction 3.7 convert in matter. A back-to-back electron-positron pair can be produced from reaction 3.6 as well and in two ways: (a) the pion decays into two photons, one of which converts in matter; (b) the pion undergoes Dalitz decay ($\pi^0 \rightarrow e^+e^-\gamma$). In both cases, the original photon has to convert and one photon from the pion decay has to be undetected. A similar reasoning applies to reaction 3.5.

The probability of $\pi^0\pi^0$ and $\pi^0\gamma$ to simulate $\gamma\gamma$ has been measured in E-760 with Monte Carlo techniques (Armstrong et al. 1997); the corresponding cross sections ($\sigma'_{\pi^0\pi^0}$ and $\sigma'_{\pi^0\gamma}$, respectively) dominate over the $\bar{p}p \rightarrow \gamma\gamma$ continuum cross section. The low probability of not detecting two photons from $\pi^0\pi^0$ is compensated by the high $\bar{p}p \rightarrow \pi^0\pi^0$ cross section, making these two background sources approximately equal; their sum is reported in Table 3.3 for some energy points.

The probability of a photon to convert before hodoscope H1, and thus to be able to fire the first-level trigger, has been measured in a sample of $\pi^0\pi^0$ events collected with a special total-energy neutral trigger with no hodoscope veto (Appendix A); it is $\eta < 1.7\times10^{-2}$, and it is consistent with estimates that employ the thickness of the material between the interaction region and H1. The probability of a pion to decay through the Dalitz process is $\delta = 1.2\times10^{-2}$.

Due to their small opening angle, electron-positron pairs might be misidentified as single electron tracks. I estimate the rejection power of the Electron-Weight cut on a sample of "pairs", defined as charged tracks with a large energy deposit in the CCAL that, combined with another calorimeter cluster, give a π^0 invariant mass. The EW distribution for events in which both candidate electrons are actually pairs is shown in Figure 3.18a, for data taken at $\sqrt{s}$=3.0 GeV. From that distribution, I deduce that the probability ω of an event with two back-to-back pairs of passing the EW cut is $\omega < 4\times10^{-2}$ (Figure 3.18b).

Following the above discussion, the expected background cross section

$\sqrt{s}$ (GeV)	$\sigma'_{\pi^0\pi^0} + \sigma'_{\pi^0\gamma}$ (pb)
2.9	1×10^3
3.1	4×10^2
3.5	6×10^1
4.3	$<6\times10^1$

Tab. 3.3: Cross sections for $\pi^0\pi^0$ or $\pi^0\gamma$ final states simulating $\gamma\gamma$ (two or one photons not detected, respectively), based upon E-760 data and Monte Carlo calculation (Armstrong et al. 1997)

due to processes 3.5, 3.6 and 3.7 is:

$$\sigma_p < \omega \cdot \Big[\begin{array}{lll} (\delta + 2\eta)^2 & \sigma'_{\pi^0\pi^0} & + \\ (\delta + 2\eta)\eta & \sigma'_{\pi^0\gamma} & + \\ \eta^2 & \sigma_{\gamma\gamma} & \end{array} \Big]. \tag{3.8}$$

Numerically, σ_p is less than 6×10^{-2} pb at 2.9 GeV and less than 3×10^{-3} pb at 3.5 GeV.

(b) Two-body Hadronic Processes

A two-body hadronic final state can simulate an e^+e^- final state if the Čerenkov gives a signal, a hadronic shower is generated in the CCAL with the characteristics of an electromagnetic shower (energy and shape) and if the kinematics is similar. Because of its high cross section and due to the relatively small mass of the pions, the process:

$$\bar{p}p \to \pi^+\pi^- \tag{3.9}$$

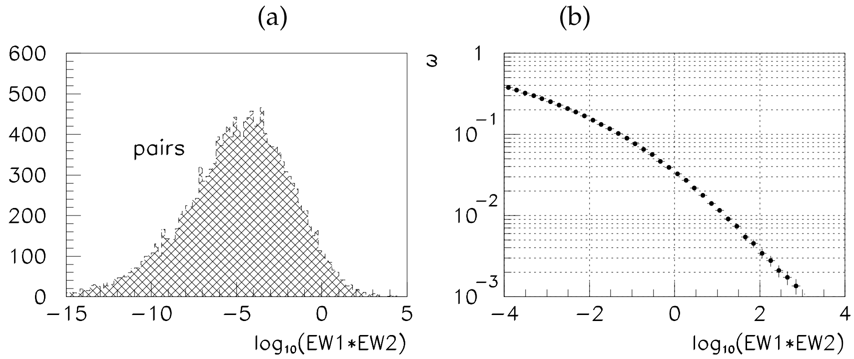

Fig. 3.18: (a) Distribution of the EW index for events with two back-to-back electron-positron pairs. (b) Rejection power ω as a function of the EW cut for the same sample of events.

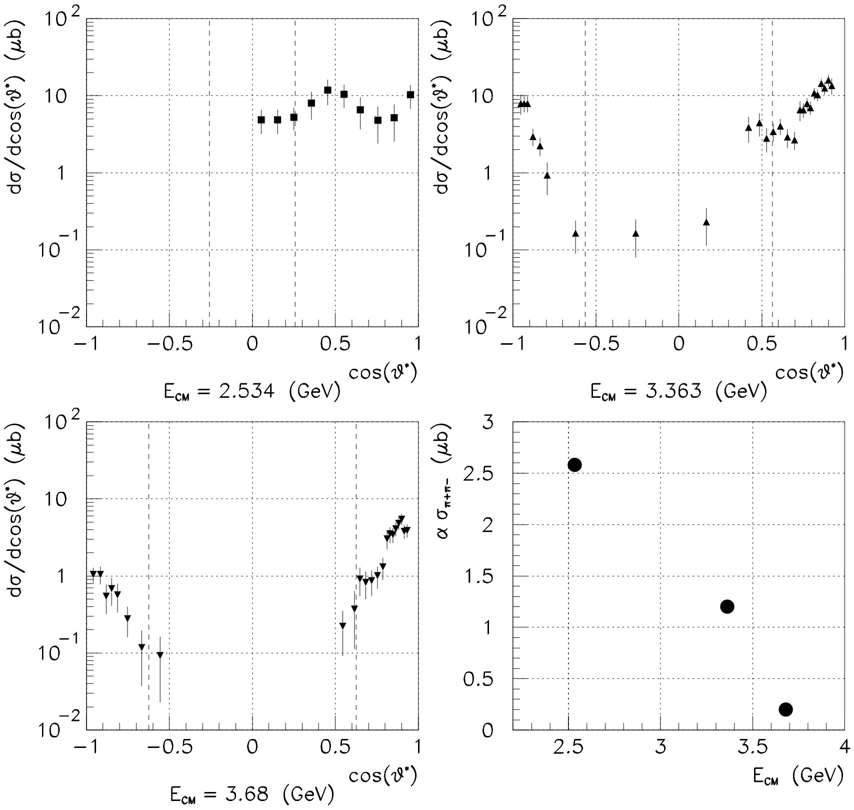

Fig. 3.19: Differential $\bar{p}p \rightarrow \pi^+\pi^-$ cross section taken from the literature (Fields et al. 1972; Eide et al. 1973; Buran et al. 1976). The bottom right plot shows the cross section integrated over the E-835 fiducial volume (vertical dashed lines in the other three plots), as a function of CM energy.

is the most relevant. I estimate the probability ξ of a hadronic shower being generated in the CCAL with an energy compatible with the e^+e^- hypothesis with data from a dedicated trigger (Appendix B). This trigger requires two charged tracks as defined by the hodoscopes, without any requirements on the Čerenkov counter or the CCAL; the result is ξ=1×10^{-2}. From the same sample of data, the rejection inefficiency of the Čerenkov contribution to the Electron-Weight cut comes out to be κ <5×10^{-3} per track.

The differential cross section of process 3.9 is shown in Figure 3.19 for three different CM energies, as measured by Fields et al. (1972), Eide et al. (1973) and Buran et al. (1976), respectively. Also shown is the cross section integrated over the acceptance α_{acc} of the E-835 detector, as a function of energy; it varies between 2 μb at 2.9 GeV and 0.5 μb at 3.6 GeV. The expected background is

$$\begin{aligned} \sigma_h &= (\alpha_{acc}\sigma_{\pi^+\pi^-}) \cdot \kappa^2 \cdot \xi^2 \qquad (3.10) \\ &< 0.5 \times 10^{-2} \text{ pb (at 2.9 GeV)} \\ &< 1.3 \times 10^{-3} \text{ pb (at 3.6 GeV).} \end{aligned}$$

(c) Inclusive Production of J/ψ

Above a certain threshold, the process $\bar{p}p \to J/\psi + X$, followed by $J/\psi \to e^+e^-$, can fit the e^+e^- two-body kinematics, when X is not detected. For this reason, data taken in proximity of some charmonium resonances have been excluded, for this analysis, from the data sample (Section 3.1). The remaining J/ψ-inclusive continuum within the acceptance of this experiment is less than 5 pb and is mainly due to $\bar{p}\,p \to J/\psi\pi^0 \to (e^+e^-) + (\gamma\gamma)$ (Armstrong et al. 1992a). The probability, for an inclusive event, of satisfying two-body kinematics has been evaluated at the χ_{c1} and χ_{c2} resonances, in

$J/\psi + \gamma$ decays in which the photon is not detected. It is defined as the fraction of events which satisfy the two-body kinematic fit probability cut. The result is $5{\times}10^{-3}$ and is taken as an upper limit for all inclusive processes in the whole energy range. This yields a background contribution σ_i smaller than $2.5{\times}10^{-2}$ pb.

Summing all the contributions $\sigma_B = \sigma_p + \sigma_h + \sigma_i$, one obtains $\sigma_B{=}9{\times}10^{-2}$ pb at 2.9 GeV and $\sigma_B{=}4{\times}10^{-2}$ pb at 3.5 GeV, corresponding to approximately one event at both energies. Since these background estimates are conservative, no subtraction from the number of candidate events is performed.

3.5 Measurement of the Form Factor

(a) Method

The number N of events collected with an integrated luminosity L and an overall efficiency ε is

$$N = \varepsilon\ L\ \sigma_{acc}, \tag{3.11}$$

where the term σ_{acc} is the differential cross section integrated over the CM acceptance region (derived from Equation 1.25):

$$\sigma_{acc} \equiv \int_{-|\cos\theta^*|_{max}}^{+|\cos\theta^*|_{max}} \left[\frac{d\sigma}{d(\cos\theta^*)}\right] d(\cos\theta^*) \tag{3.12}$$

$$= \frac{\pi\alpha^2}{8EP} \cdot \left[A \cdot |G_M|^2 + \frac{4m_p^2}{s} \cdot B \cdot |G_E|^2\right]. \tag{3.13}$$

At different values of s, the fiducial range $15° < \theta < 60°$ used in the event selection corresponds to different acceptances for θ^*, the scattering angle in the CM frame. At $\sqrt{s} < 3.661$ GeV, it is the upstream edge of the fiducial range ($\theta = 60°$) that determines $|\cos\theta^*|_{max}$; whereas, for $\sqrt{s} > 3.661$ GeV, it is the downstream edge ($\theta = 15°$) that constrains the acceptance. The fact that the E-835 apparatus cannot distinguish between electrons and positrons is taken into account by integrating from $-|\cos\theta^*|_{max}$ to $+|\cos\theta^*|_{max}$; the (energy-dependent) acceptance coefficients A and B are:

$$A \equiv 2 \cdot \int_0^{|\cos\theta^*|_{max}} \left(1+\cos^2\theta^*\right) d(\cos\theta^*) \tag{3.14}$$

$$B \equiv 2 \cdot \int_0^{|\cos\theta^*|_{max}} \left(1-\cos^2\theta^*\right) d(\cos\theta^*). \tag{3.15}$$

For small $|\cos\theta^*|_{max}$, A is approximately equal to B and the relative importance of the 'electric' and 'magnetic' contributions is weighed by $4m_p^2/s$ only. As $|\cos\theta^*|_{max}$ approaches one, the ratio A/B tends to 2, and the 'electric' contribution is further suppressed.

The measurement of the angular distribution of the form factor events would decouple the 'electric' and 'magnetic' contributions to the differential cross section. Unfortunately, high statistics and wide angular coverage are necessary. Figure 3.20 gives an idea of how close three of the possible angular distributions are. A flat distribution (solid line), a $1+\cos^2\theta^*$ distribution (dashed line, implying negligible 'electric' contribution) and a $1-\cos^2\theta^*$ distribution (dotted line, negligible 'magnetic' contribution) are fitted to the data in the CM acceptance region common to all data points ($|\cos\theta^*| < 0.45$, from Table 3.4). The small number of events makes it impossible to discriminate between the various functional forms, which are equally compatible with the data; $\chi^2 \simeq 0.8$ for all three fits.

Since the low statistics and the limited $\cos\theta^*$ range do not allow to make a separate measurement of $|G_E|$ and $|G_M|$, I make two alternative hypotheses: (a) $|G_E| = |G_M|$, as is the case at the threshold of the timelike region ($s = 4m_p^2$), by definition of form factors (Equation 1.11); (b) the 'electric' contribution is assumed to be negligible. Under hypothesis (b), the measurement of the magnetic form factor of the proton is achieved through the

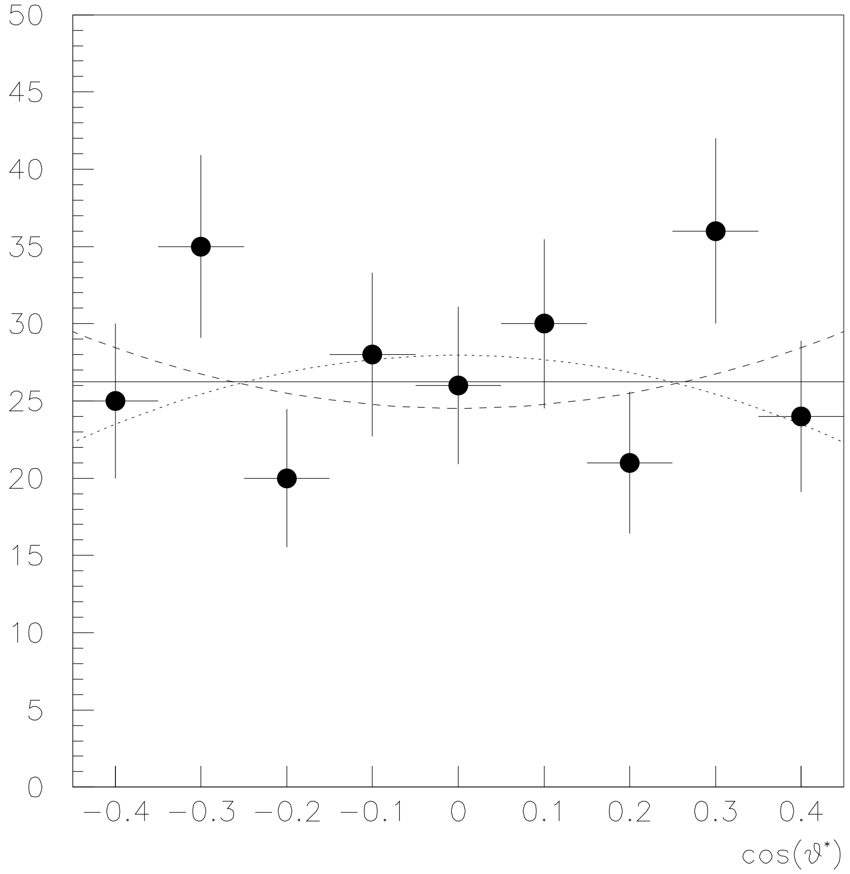

Fig. 3.20: Angular distribution of all form factor events in the CM acceptance region common to all energy points (two entries per event). Different functional forms are equally compatible.

relation:

$$|G_M| = \frac{1}{\alpha} \cdot \sqrt{\frac{8}{\pi}} \cdot \left[\frac{E\,P\,N}{\varepsilon\,A\,L}\right]^{\frac{1}{2}} . \tag{3.16}$$

Under hypothesis (a), A is replaced by $A + (4m_p^2/s) \cdot B$.

(b) Results

The results obtained are shown in Table 3.4. For each energy region, the integrated luminosity L, the number of selected events N, the cross section $\sigma_{acc} \equiv N/(L \cdot \varepsilon)$ and the geometrical acceptance in the CM frame are shown. Both statistical and systematic errors on σ_{acc} and $|G_M|$ are reported. The magnitude of the observed cross sections σ_{acc} relative to the total $\bar{p}p$ cross section (≈ 70 mb) should be emphasized.

Some data have been taken at $s = 18.4$ GeV^2, but no e^+e^- events have been observed. In Table 3.4, an upper limit of 2.44 events is given, corresponding to a 90% confidence level (Feldman and Cousins 1998; Caso et al. 1998).

The values of $|G_M|$ determined in the two hypotheses differ by 16% at $s = 8.8$ GeV^2 and by 9% at $s = 14.4$ GeV^2. The values of $|G_M|$ obtained under assumption (a) are plotted in Figure 3.21 and in Figure 3.22, where they are compared with the E-760 results and with earlier measurements.

Figure 3.21 shows a fit to the data in the asymptotic form described by Equation 1.30, where C and Λ are treated as free parameters. The fit can reproduce the data very well ($\chi^2 = 0.3$), even though the asymptotic regime has not been reached. In fact, there is still an appreciable difference between the timelike and the spacelike form factors. In Figure 3.21, the spacelike form factor at $s = Q^2$ is represented by the dipole functional form (Equation 1.16); the timelike form factor is 1.5 to 3 times larger, depending upon the energy.

s	L	N	σ_{acc}	$\lvert\cos\theta^*\rvert_{max}$	$10^2 \times \lvert G_M\rvert$	
(GeV^2)	(pb^{-1})		(pb)		(a)	(b)
8.84 ± 0.16	17.69	93	$7.78^{+0.81+0.96}_{-0.81-0.67}$	0.451	$3.55^{+0.18+0.22}_{-0.19-0.17}$	$4.13^{+0.21+0.25}_{-0.22-0.18}$
10.78 ± 0.28	1.78	3	$2.5^{+1.9+0.3}_{-1.6-0.2}$	0.544	$2.11^{+0.70+0.14}_{-0.83-0.11}$	$2.38^{+0.78+0.15}_{-0.94-0.11}$
12.43 ± 0.02	47.84	33	$1.02^{+0.18+0.13}_{-0.18-0.09}$	0.601	$1.42^{+0.12+0.08}_{-0.13-0.06}$	$1.57^{+0.13+0.09}_{-0.14-0.07}$
13.11 ± 0.18	33.99	14	$0.61^{+0.19+0.07}_{-0.16-0.05}$	0.621	$1.11^{+0.16+0.07}_{-0.16-0.05}$	$1.22^{+0.18+0.08}_{-0.17-0.06}$
14.36 ± 0.50	1.86	1	$0.80^{+1.4+0.1}_{-0.5-0.1}$	0.604	$1.37^{+0.90+0.13}_{-0.54-0.11}$	$1.50^{+0.99+0.14}_{-0.59-0.12}$
18.40 ± 0.01	0.76	0	< 4.78	0.508	< 4.36	< 4.69

Tab. 3.4: Summary of the results of the form factor analysis.

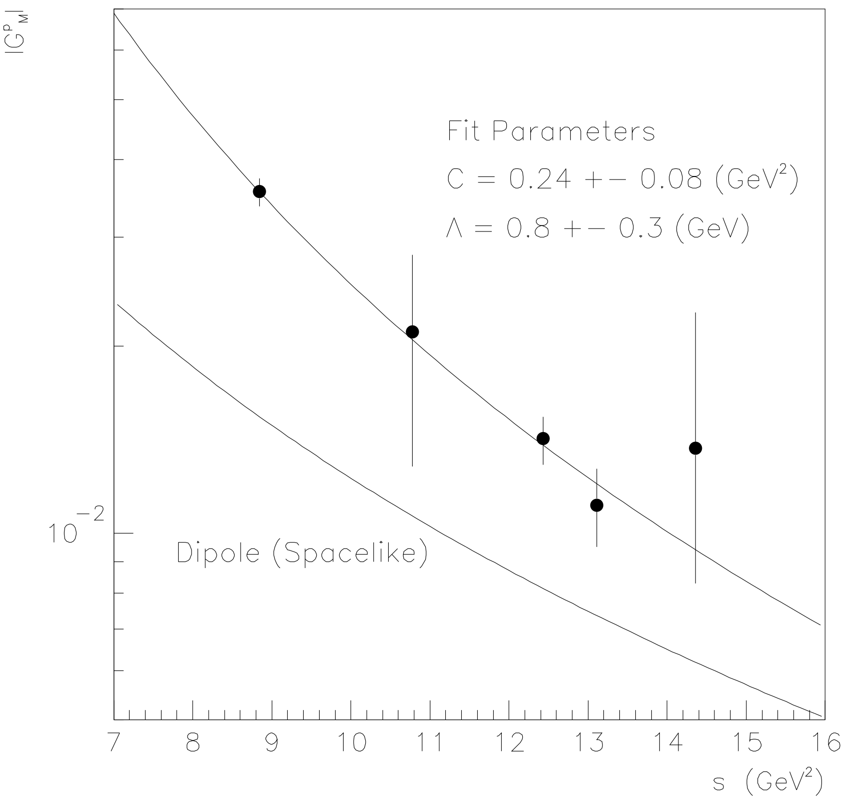

Fig. 3.21: A fit to the data in the asymptotic form of Equation 1.30. Also shown is the dipole behavior of the form factor in the spacelike region.

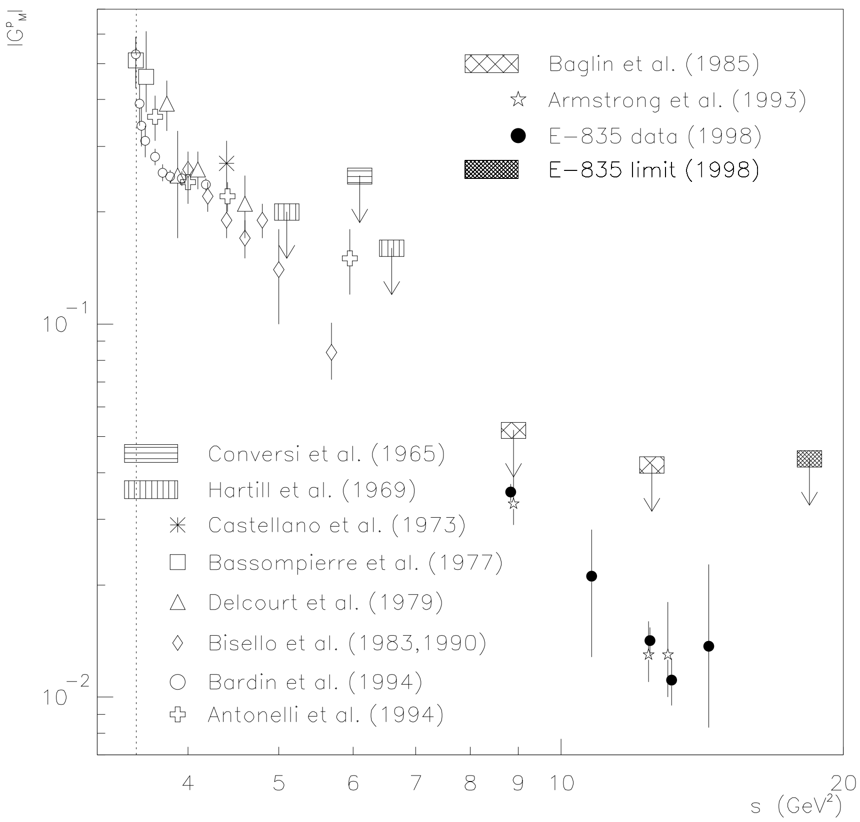

Fig. 3.22: The measurements presented in this dissertation (E-835 data and limit) are compared with all previous measurements. The values correspond to the $|G_E| = |G_M|$ hypothesis. The cross-hatched rectangles represent upper limits at the 90% confidence level.

(c) Remarks on the Uncertainties

Both statistical and systematic uncertainties on $|G_M|$ are reported in Table 3.4. They come from the errors on the directly-measured quantities, namely the number of events N, the luminosity L, the selection efficiency ε and the CM energy $\sqrt{s}$ (Equation 3.16).

In some cases, the relative errors on the directly-measured quantities are not small compared to 1, especially when coming from the number of events. For this reason, when propagating the error on x (one of the directly-measured quantities) to the derived variable $|G_M| = f(x) \propto \sqrt{x}$, I used the exact formula $\delta |G_M| = f(x + \delta x) - f(x)$ instead of the approximation $\delta |G_M| = (d |G_M| / dx) \cdot \delta x$.

Statistical Error. The statistical uncertainties dominate over the systematic ones, except for the data point where there are 93 events. Obviously, they are mainly due to the error on N. There is also a small contribution from the measurement of the efficiency (0.3%) and of the luminosity (0.1%). For the purpose of calculating the statistical error on the form factor, the contributions from the various sources are added in quadrature.

Systematic Error. The main systematic uncertainty comes from the efficiency (3–4%). The error on the value of ε used for all six data points takes into account variations due to CM energy, run to run inhomogeneities and background subtraction procedure, described in Section 3.2. The systematic uncertainty on the luminosity L (3%) yields a relative error of 1.5% on the form factor. The error on E, P, A and B, due to the grouping of several runs at different energies, is generally negligible, except for the point at s = 14.4 GeV^2, where the form factor is small and the energy interval is relatively wide; there, the corresponding relative error on $|G_M|$ is 4%. Systematic uncertainties are added linearly when calculating the total systematic error on the form factor.